Chemical Engineering Journal 151 (2009) 308–318

Contents lists available at ScienceDirect

Chemical Engineering Journal

journal homepage: www.elsevier.com/locate/cej

Hydroconversion of n-heptane over Pt/Al-MCM-41 mesoporous molecular sieves

Dapeng Liu[a], Shuangquan Hu[a], Raymond Lau[a], Armando Borgna[b], Gary L. Haller[c], Yanhui Yang[a,*]

[a] School of Chemical and Biomedical Engineering, Nanyang Technological University, Singapore 637459, Singapore
[b] Institute of Chemical Engineering and Sciences, A*STAR (Agency for Science, Technology and Research), 1 Pesek Road, Jurong Island, Singapore 627833, Singapore
[c] Department of Chemical Engineering, Yale University, 208286, New Haven, CT 06520-8286, United States

ARTICLE INFO

Article history:
Received 15 September 2008
Received in revised form 3 March 2009
Accepted 30 March 2009

Keywords:
Pt/Al-MCM-41
n-Heptane hydroconversion
Curvature effect

ABSTRACT

Pt/Al-MCM-41 samples with constant metal loading but various pore sizes were hydrothermally synthesized using cetyltrimethylammonium bromide (CTAB) surfactant with different alkyl chain length (pore diameters ranging from 1.7 to 2.7 nm). These samples were carefully characterized by X-ray diffraction, N_2 physisorption, the infrared spectra, temperature-programmed desorption of ammonia, and solid-state MAS NMR. Hydroconversion of n-heptane was carried out over these Pt/Al-MCM-41 samples. It was found that the steric restrictions are negligible for this catalytic system and high catalytic activity and high isomer yield were achieved. Another finding was that the radius of curvature of pore wall surface had effect on the hydroconversion of n-heptane. It was speculated that the main reason for the curvature effect in this particular model system was that the formation of alkylcarbenium ions, also denoted as the transfer of proton, was affected by the distribution of acid sites on the pore wall surface.

1. Introduction

Hydroconversion of straight-chain paraffins plays a crucial role in the oil refining industry to enhance the octane number of gasoline, to improve the low temperature performance of diesel, and to produce lube oils with a high viscosity index [1,2]. Zeolite-based bifunctional catalysts attract more attention than the traditional chlorided alumina-type catalysts because the former are more robust and able to withstand certain impurities such as water and sulfur in the feedstock. Early developed zeolite supported noble metal catalysts showed effective catalytic performance for n-pentane and n-hexane isomerization; SAPO-11 exhibited high isomerization selectivity during processing high alkanes (C_7^+) [3–9]. However, the presence of the less accessible active centers and unsuitable acidity over these materials, restrict practical applications of zeolite catalysts.

The discovery of the M41S family of mesoporous materials with characteristics such as long-range order, high surface areas and tailorable pore sizes, have opened up new possibilities in the fields of adsorption, separation, and heterogeneous catalysis [10–12]. Comparable or improved catalytic properties for various reactions have been reported with mesoporous molecular sieves [11,12].

The effect of the pore structure on heterogeneous catalytic reaction is an interesting topic of great importance. With microporous zeolite catalysts, numerous catalytic phenomena were rationalized by the well-known concept of shape selective catalysis [13–18]. However, the transport limitations and restricted transition state selectivity in zeolites always made the question of shape selectivity perplexing. Moreover, it was rather difficult to associate the catalytic effect directly with the radius of curvature of microporous materials because a suitable zeolite with different pore sizes as well as unchanged composition and structure cannot be found readily [19].

For the nano-porous channel of M41S materials, due to the small sizes of the guest molecules compared with the host channel of mesoporous materials generally, it is more precise to elucidate the relevant experimental behaviors by the surface curvature effect. Although the radius of curvature changes in mesoporous MCM-41 material is small compared with the microporous zeolites, significant effects on physicochemical characteristics and catalytic properties indeed have induced by this variation in local geometry. Feng et al. [20] recognized that the relative acidity estimated by the isomerization selectivity of 2-methyl-2-pentene on Al-MCM-41 varied with pore size. Catalytic results on n-hexane dehydrocyclization with Pt/K-MCM-41 indicated both the reaction rate and benzene selectivity decreased markedly as the pore size increases [21]. The formation of the cobalt clusters with specific sizes in Co-MCM-41 was successfully achieved by changing the pore size of catalyst, which could be used in growing uniform-diameter single-walled carbon nanotubes controllably [22]. Most recently, Yang et al. observed a more convincing pore wall curvature effect in

* Corresponding author at: School of Chemical and Biomedical Engineering, Nanyang Technological University, 62 Nanyang Drive, N1.2-B1-18, Singapore 637459, Singapore. Tel.: +65 6316 8940; fax: +65 6794 7553.
E-mail address: yhyang@ntu.edu.sg (Y. Yang).

1385-8947/$ – see front matter © 2009 Elsevier B.V. All rights reserved.
doi:10.1016/j.cej.2009.03.052

methanol oxidation over V-MCM-41, clearly showing that activity and selectivity depend strongly on the pore diameter ranging from 1.7 to 2.9 nm [23]. It was suggested that the curvature dominates the reduction stability of V species in V-MCM-41, thus leading to the difference of reaction performances. Even in liquid reaction, a considerable curvature effect existed on the initial activity for cyclohexene epoxidation over V-MCM-41 [24].

In this work, the hydroconversion of n-heptane is carried out over Pt/Al-MCM-41 catalysts with constant metal loading but various pore diameters. The effect of radius of curvature on the diffusion and catalytic activity is investigated. The possible mechanism of the curvature effect on the catalytic reactivity is discussed.

2. Experimental

2.1. Catalyst preparation

Sources of silica were Cab-O-Sil M-5 fumed silica (Riedel-de Haën) and tetramethylammonium silicate solution (15–20 wt.% in H_2O, Aldrich). The aluminum source was aluminum isoproxide (Alfa Aesar, 98%). Alkyltrimethyl ammonium surfactants, $C_nH_{2n+1}(CH_3)_3N^+Br^-$ with $n = 10$, 12, 14 (Alfa Aesar) and with $n = 16$ (Sigma) were used as structure directing agents. One antiforming agent, Antiform A (Sigma) which is a silane polymer alkyl terminated by methoxy groups, was used to remove excess foam and improve the solubility of the gel [25].

The aluminosilicate MCM-41 samples with two Si/Al molar ratios of 25 and 125 were hydrothermally synthesized according to the following procedures. Tetramethylammonium silicate was mixed with water followed by adding fumed silica. Two drops of antiform A was introduced before adding the surfactant solution. After 1 h of magnetic stirring, the Al source was added. The mixture was aged for 1 h under stirring and transferred into a Teflon-lined stainless steel autoclave. The corresponding molar composition of the gel mixture was $50SiO_2{:}Al_2O_3{:}7(C_nTMA)_2O{:}3(TMA)_2O{:}3000H_2O$. The mixture was then heated statically under autogenous pressure at 120 °C for 48 h. After crystallization, the solid product was recovered by filtration, washed extensively with deionized water and dried in air under ambient temperature. The pre-dried sample was calcined at 540 °C for 6 h under flowing air to remove the surfactant. The calcined sample was ion-exchanged three times with 0.5 M of NH_4NO_3 solution at 80 °C for 6 h. The ion-exchanged product was dried at 80 °C overnight and then calcined at 450 °C for 4 h to obtain the acidic form of MCM-41. In this work, the materials are designated as C*n*-*X*, where *n* indicates the number of carbon atoms in the alkyl chain of the surfactant and X the Si/Al molar ratio.

Platinum supported catalysts with 0.8 wt.% Pt loading were prepared by impregnating the acidic MCM-41 with aqueous $H_2PtCl_4{\cdot}6H_2O$ solution using incipient wetness impregnation method. The impregnated catalysts were dried at 80 °C overnight. Air oxidation and hydrogen reduction of the supported catalysts were completed in situ before the catalytic tests.

2.2. Catalyst characterization

XRD patterns were recorded on Bruker D8 advance powder diffractometer operated at 40 kV and 40 mA, using monochromatic Cu Kα radiation with 0.02° step size and 2 s step time within the 2θ range of 1–8°.

Nitrogen adsorption–desorption isotherms were measured at −196 °C with a static volumetric Quantachrome apparatus. Before the adsorption experiments, the calcined samples were degassed at 250 °C under vacuum overnight. The pore size distributions were evaluated from the desorption branch of isotherms using the BJH method [26].

Transmission electron microscopy (TEM) was conducted on a JEOL JEM-2010 operated at 200 kV. Before observation, the samples were suspended in ethanol and dried on holey carbon-coated Cu grids. Scanning electron microscopy (SEM) was performed on a JEOL-6300F microscope using conventional sample preparation and imaging techniques.

The infrared (IR) spectra in the framework range of 400–1400 cm^{-1} were recorded on a Digilab FTS 3100 spectrometer with a resolution of 0.5 cm^{-1}, using the KBr wafer technique.

Solid-state MAS NMR spectra were recorded at room temperature on a Bruker AMX400 spectrometer. Tetramethylsilane (TMS) and aluminum nitrate were used as references for ^{29}Si and ^{27}Al NMR measurements.

The temperature-programmed desorption (TPD) of ammonia was used to measure the acidic properties of the MCM-41 materials. The sample was activated at 500 °C for 1 h under flowing helium and then cooled to 120 °C before introducing anhydrous ammonia (5% in helium) for 30 min. Subsequently the physisorbed ammonia was removed by flushing with helium during 2 h at 120 °C. The thermal desorption was conducted in flowing helium from 150 to 600 °C using a heating rate of 8 °C min^{-1}. Ammonia desorption was monitored continuously with a thermal conductivity detector. The outlet gas was passed through a 0.01-M H_2SO_4 solution to adsorb the released NH_3. After adsorption, the solution was back-titrated to obtain total amount of desorbed ammonia.

2.3. Catalytic reactions

The hydroconversion of *n*-C7 was performed at atmospheric pressure in a continuous-flow fixed-bed microreactor loaded with 0.2 g of catalyst (40–60 mesh). The inner diameter of straight quartz reactor is about 3 mm and the loading length of catalyst diluted with appropriate amount of inert quartz particles is 45 mm to ensure the reaction can be conducted under plug flow condition. Prior to the reaction, the sample was activated in situ under flowing air at 450 °C during 2 h and reduced at 400 °C in flowing hydrogen for 1 h. After reduction, the reactor was then cooled to the desired reaction temperature. The liquid *n*-C7 was pumped into a vaporizer and mixed with a hydrogen flow at 140 °C. The mixture was then fed into the reactor. The molar ratio of H_2/*n*-C7 and the WHSV were 25 and 1.8 h^{-1}, respectively. The reaction products were periodically analyzed by on-line gas chromatograph (GC) equipped with a HP-PONA capillary column (50 m × 0.2 mm) and a flame ionization detector (FID).

3. Results and discussion

3.1. Physicochemical characterization

Mesoscopic ordering of the calcined MCM-41 products was examined using powder X-ray diffraction (XRD) and results are displayed in Fig. 1. The XRD patterns of various Al-MCM-41 samples show typical reflections of hexagonally one-dimensional MCM-41 structure. As the surfactant chain length decreases, the main (1 0 0) diffraction peak gradually shifts to higher angles, indicating the decrease of unit cell parameters. The quality of samples, estimated through the full width at half maximum (FWHM) of the main diffraction peak in the 2θ region of 1–8°, increases with increasing the carbon chain of the surfactant. Physicochemical properties of the calcined samples are summarized in Table 1. As previously reported [27], the unit cell parameter and the pore size decrease as the surfactant chain length decreases. The BET surface area and pore volume increase with decreasing the aluminum content. All samples exhibit large specific surface areas (greater than 1000 $m^2\ g^{-1}$). According to the values reported in Table 1, no clear correlation

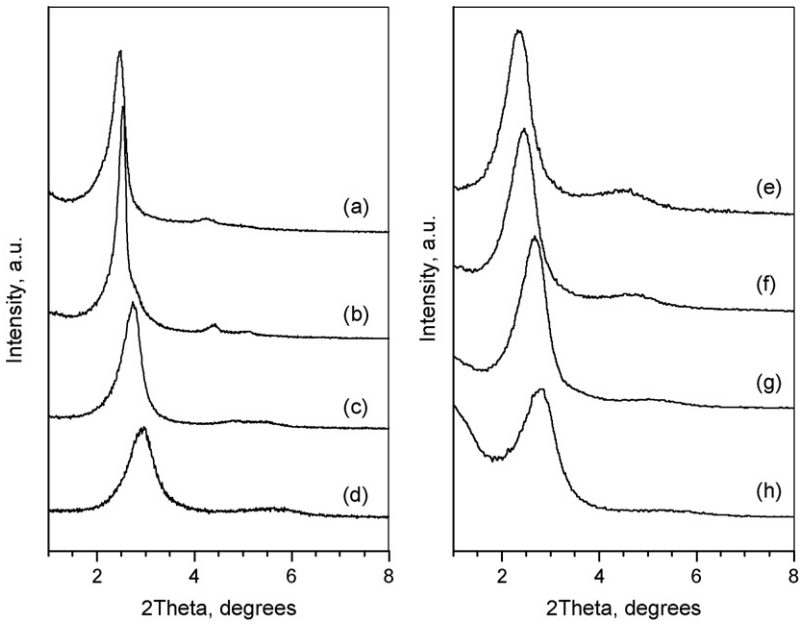

Fig. 1. XRD patterns of calcined Al-MCM-41 samples (a) C16-25, (b) C14-25, (c) C12-25, (d) C10-25, (e) C16-125, (f) C14-125, (g) C12-125 and (h) C10-125.

between the physical properties and the Al content can be established.

Fig. 2 illustrates the type IV nitrogen physisorption isotherms [28] and pore size distribution for the calcined MCM-41 samples. All samples exhibit a sharp step of the nitrogen uptake at relative pressures of 0.12–0.36 which is originated from the capillary condensation of nitrogen inside the primary mesopores. In addition, the small hysteresis loop at relative pressures >0.9 was attributed to the condensation of nitrogen in the secondary pores such as depressions of rough surfaces or intercrystallite voids in aggregates [29,30]. This observation is more pronounced for the samples with Si/Al ratio of 125. It can also be observed that the pore size increases regularly as the alkyl carbon chain length of surfactant increases, in good agreement with previous reports [10,27].

The morphology and mesostructure of a typical Al-MCM-41 sample, C14-125, are illustrated in Fig. 3(A) and (B), respectively. It is clear from SEM image that the agglomerates are generated from numerous tiny primary particles; nevertheless, we observed the irregular shapes and a wide particle size distribution for the secondary particles as commonly encountered in the conventional surfactant-templated mesoporous materials [31]. TEM image reveals the presence of the regular array of mesoporous channels in a hexagonal arrangement, which is in agreement with previous report [10].

The mid-infrared spectra of calcined Al-MCM-41 samples and amorphous silica (Cab-O-Sil) are presented in Fig. 4(A), while the relationship of the asymmetric stretching vibrations and pore size is shown in Fig. 4(B). The assignments of IR vibrational modes can be obtained following the empirical interpretations of the mid-infrared spectra for synthetic zeolites proposed by Flanigen et al. [32]. For all samples, three distinct absorption bands at around 1070–1110, 803 and 460–470 cm^{-1} are assigned to the internal asymmetric stretching of TO_4 tetrahedron (T = Si or Al), the external symmetric stretching of adjacent TO_4 tetrahedron and the bending vibration of the O–T–O, respectively. Furthermore, the shoulder near 1230 cm^{-1}, clearly observed on Al-MCM-41 samples, is attributed to external asymmetric stretching modes of TO_4. As compared with amorphous silica, the appearance of relatively stronger bands on mesoporous molecular sieves is a distinct indication of the structure regularity and bonding of their framework to a large extent. The internal lattice vibrations of TO_4 tetrahedron can be viewed as T–O vibrations of isolated $TO_{4/2}$ tetrahedron of the zeolite framework. Despite their less sensitivity to variations in framework structure, these bands are sensitive to composition properties and structural characteristics such as the variation of T–O–T bond angle. Fig. 4(B) shows that the asymmetric stretching shifts to lower frequencies with pore size for each series of samples. Moreover, the overall blue-shift of the frequency is seen with increasing Al loading. This monotonic decrease of the asymmetric stretching frequency with pore size may be due to the difference of the average T–O–T bond angle caused by the variation of the pore diameter.

Table 1
Structural characteristics of Al-MCM-41 samples.

Sample	Si/Al ratio		Unit cell a_0[a], nm	Surface area, $m^2\ g^{-1}$	Pore volume, $cm^3\ g^{-1}$	Pore size, nm	Wall thickness[b], nm
	Gel	Calcined					
C16-25	25	24.2	4.16	1024	1.02	2.52	1.64
C14-25	25	23.4	4.06	1005	0.72	2.26	1.80
C12-25	25	23.1	3.68	1041	0.91	2.01	1.67
C10-25	25	21.8	3.44	1028	0.71	1.74	1.70
C16-125	125	117.1	4.37	1281	1.17	2.70	1.67
C14-125	125	114.0	4.15	1247	1.14	2.38	1.77
C12-125	125	112.1	3.81	1157	0.87	2.13	1.68
C10-125	125	103.5	3.62	1181	0.83	1.81	1.81

[a] The unit cell size in hexagonal unit cell was calculated using $a_0 = 2d_{1\,00}\sqrt{3}$.
[b] The wall thickness was obtained by subtracting the pore size from the unit cell.

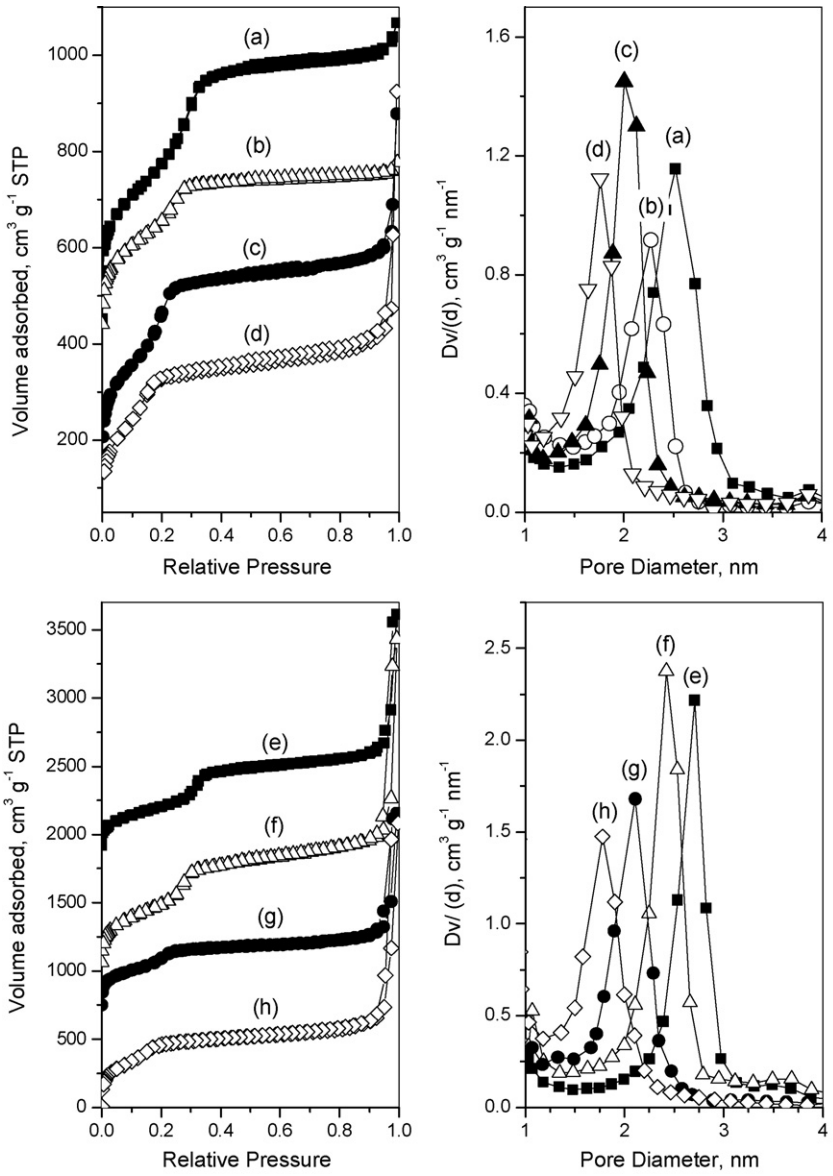

Fig. 2. Nitrogen physisorption at −196 °C for (a) C16-25, (b) C14-25, (c) C12-25, (d) C10-25, (e) C16-125, (f) C14-125, (g) C12-125 and (h) C10-125.

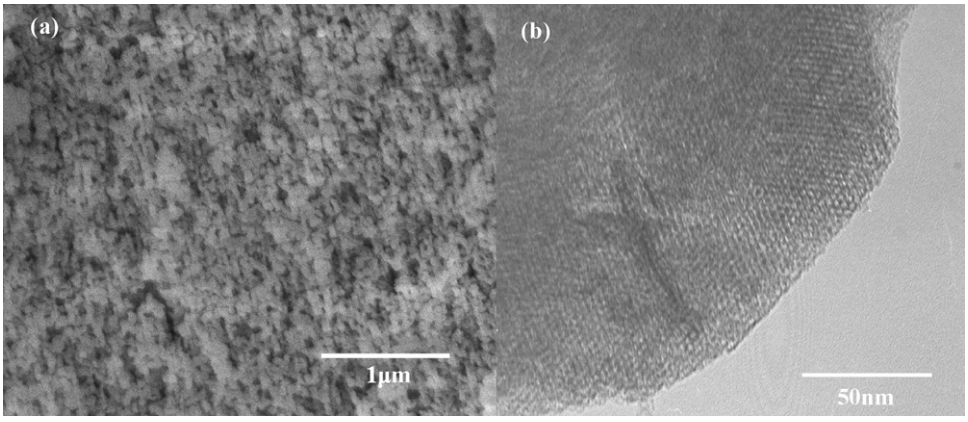

Fig. 3. SEM (a) and TEM (b) images of calcined C14-125 sample.

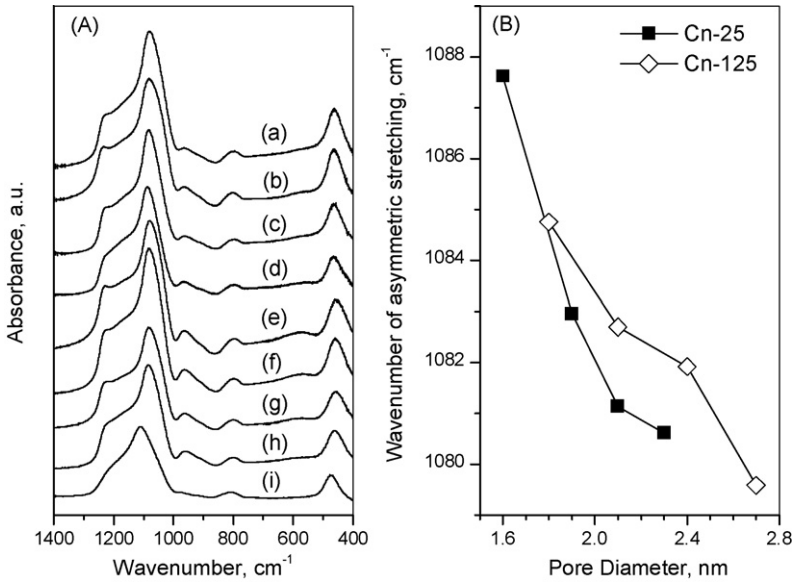

Fig. 4. (A) Mid-infrared of Al-MCM-41 samples: (a) C16-25, (b) C14-25, (c) C12-25, (d) C10-25, (e) C16-125, (f) C14-125, (g) C12-125, (h) C10-125 and (i) amorphous silica; and (B) the asymmetric stretching vibration of TO_4 as a function of pore sizes of Al-MCM-41 materials.

Fig. 5(A) and (B) illustrate the ^{27}Al MAS NMR and ^{29}Si NMR spectra of the calcined C*n*-125 series. For ^{27}Al MAS NMR, two peaks with chemical shifts of 0.7 and 54 ppm can be observed, which correspond to octahedral and tetrahedral aluminum species, respectively [33,34]. In all cases, the main peak is attributed to the tetrahedral Al. This means that most of aluminum atoms have been incorporated into the framework [35]. The non-framework, octahedral Al may be formed by framework dealumination during high-temperature calcinations [36]. Quantitative calculations indicate that more than three-fourths of aluminum remained in a tetrahedral coordination environment. The ^{29}Si MAS NMR spectra contain two major peaks between 99 and −109 ppm corresponding to two different Si species in the framework. The chemical shift of 109 ppm comes from the Q^4 [$Si(OSi)_4$] species while the peak around 99 ppm is contributed by Q^3 [$Si(OSi)_3OH$] and Q^4 [Si (3Si, 1Al)] sites, in agreement with previous reports [29,37]. The relatively stronger Q^4 signal indicates the condensation of surface silanol groups and the existence of well-ordered wall structure.

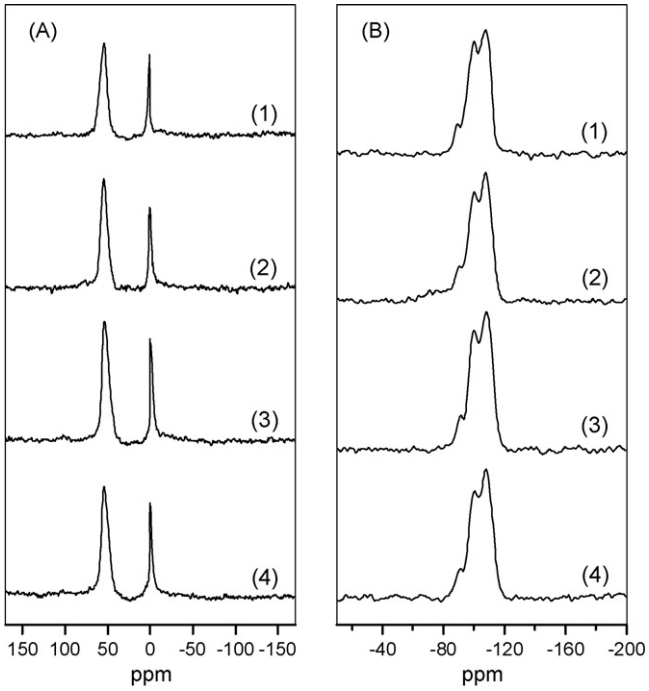

Fig. 5. ^{27}Al MAS NMR spectra (A) and ^{29}Si MAS NMR spectra (B) of Al-MCM-41 samples: (1) C16-125, (2) C14-125, (3) C12-125 and (4) C10-125.

The NH_3-TPD profiles and the acid strength distribution obtained by Gaussian deconvolution of two series of MCM-41 samples are presented in Fig. 6. Ammonia desorption occurs in the temperature range of 150–400 °C, revealing that the surface acid sites are of weak and medium strength for all samples. The low-temperature peak (below 250 °C, existing on all the samples) is related to weakly chemisorbed NH_3 molecule. The higher desorption peak (from 290 to 350 °C) is associated with medium acid sites. As expected, all C*n*-25 samples have more acid sites than C*n*-125 ones; especially the C16-25 which possesses the largest amount of adsorption sites for ammonia. Also a well-defined high-temperature shoulder near 320 °C can be seen for this sample. For C*n*-25 series, the number of total acid sites has the following sequence: C16-25 > C14-25 > C12-25 ≈ C10-25. In contrast, the total acid is very similar for all C*n*-125 samples, around 0.1 mmol g^{-1}. Concerning the distributions of two kinds of acid sites, a slight increase of medium acid sites with the pore size is shown for C*n*-25 samples; meanwhile, a higher proportion of medium acid sites exist on C12-25 and C10-25. However, the similar trends cannot be observed on C*n*-125 series, only C14-125 contains the highest proportion of medium acid sites.

3.2. Hydroconversion of n-C7

It is generally recognized that when paraffin hydroconversion is performed over solid acid supported noble metal catalysts, two critical factors affecting the catalytic performance and the final product distribution are the acidity and the pore structure of support materials, assuming that the hydrogenating/dehydrogenating function is not the limiting step. This assumption is applicable for the current catalytic system owing to the weak acidity of the mesoporous materials. Under the present experimental operations, the major reactions involved are isomerization and cracking. Usually, a minor

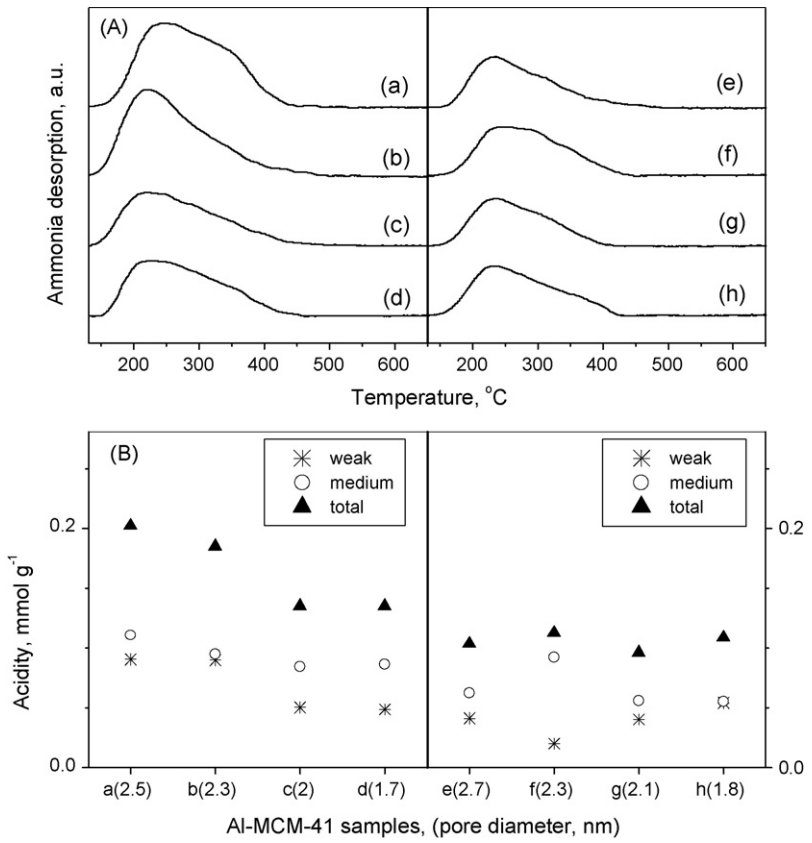

Fig. 6. NH_3-TPD characterization of Al-MCM-41 acidity (A) NH_3-TPD profiles and (B) relative acidity of the calcined samples: (a) C16-25, (b) C14-25, (c) C12-25, (d) C10-25, (e) C16-125, (f) C14-125, (g) C12-125 and (h) C10-125.

cyclization is observed, which was also reported by others using similar aluminosilicate mesoporous materials [38,39].

The total conversions and yields of various products over C*n*-25 catalysts between 300 and 360 °C are given in Fig. 7. It is observed that the *n*-C7 conversion increases as the reaction temperature increases. Samples C16-25 and C14-25 show higher catalytic conversions as compared to the samples synthesized with shorter chain surfactant. All the catalysts synthesized show higher yield to iso-

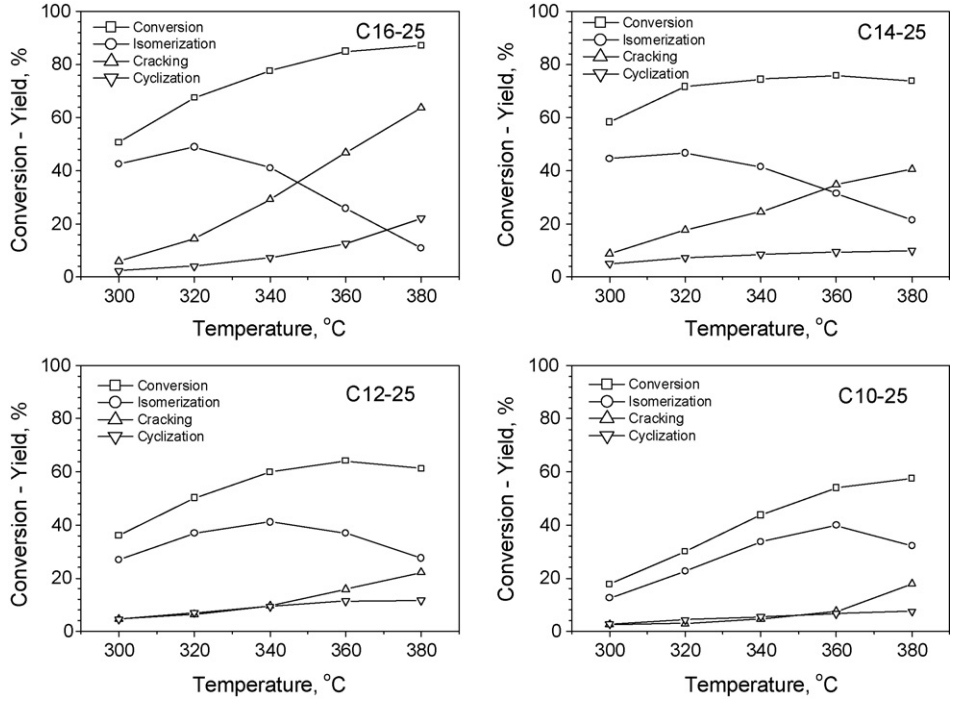

Fig. 7. *n*-C7 conversion and yields of various products vs. temperature over Pt supported C*n*-25 catalysts.

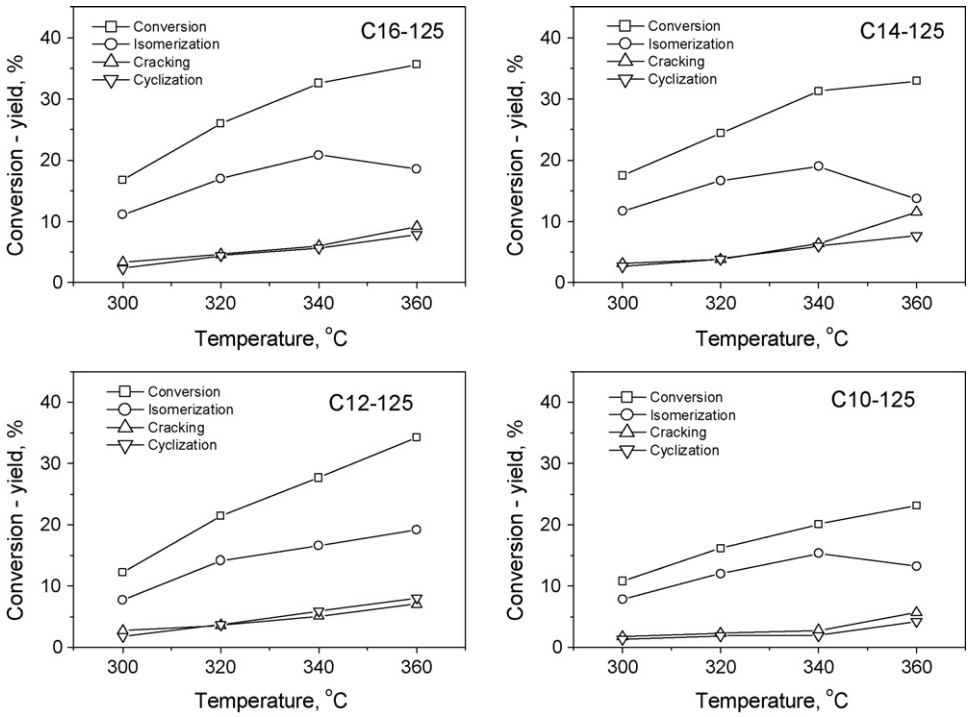

Fig. 8. *n*-C7 conversion and yields of various products vs. temperature over Pt supported C*n*-125 catalysts.

mers than cracking and cyclization regardless of the surfactant chain length used. However, the isomerization yields depend on the reaction temperature; they pass through a maximum and then decrease with the reaction temperature. This maximum is clearly observed for the samples derived from surfactants with longer carbon chain, especially for the C16-25 sample. The opposite trend is observed for cracking and cyclization products; more cracking and cyclization occur at higher temperature due to the thermodynamic limitation of the isomerization reaction [40] and the higher activation energy for these reactions. For C10-25 sample, a volcano curve is observed with the highest isomerization yield occurs at 360 °C whereas the cracking and cyclization are relatively low and constant below 360 °C. Different catalytic performances are observed when the Si/Al ratio of Al-MCM-41 is varied from 25 to 125; all C*n*-125 catalysts show poorer conversions and yields than C*n*-25, which is probably due to the lower acid characteristics as compared to C*n*-25 (see Fig. 8). For C12-125 catalyst, it shows a slight monotonic increase of isomer yield against temperature. This is caused by

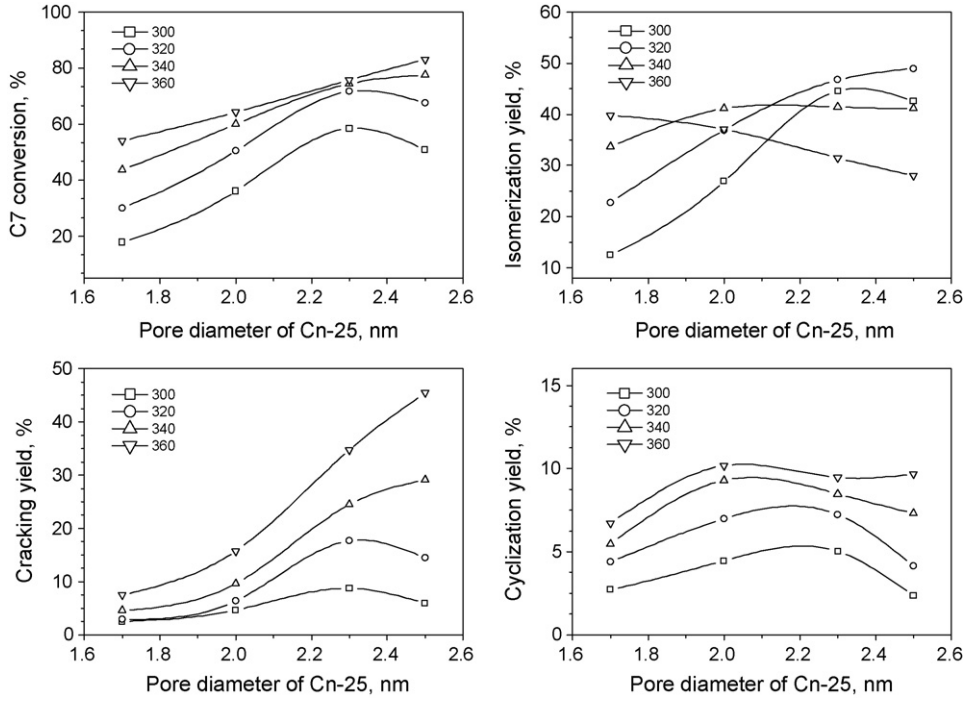

Fig. 9. Influence of pore size of C*n*-25 catalysts on *n*-C7 conversion and yields of various products.

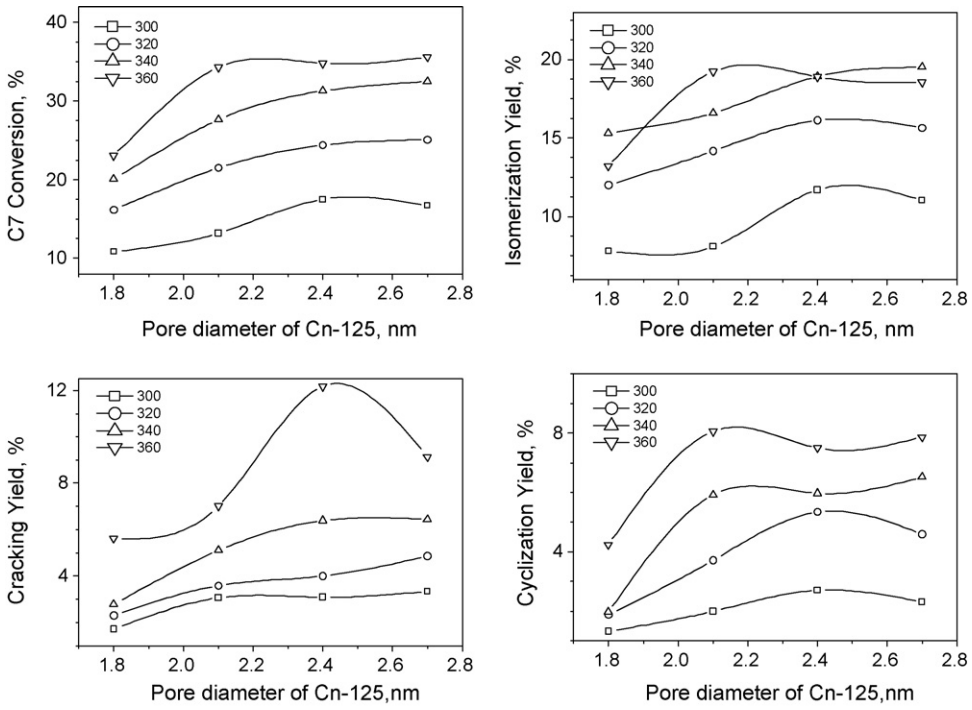

Fig. 10. Influence of pore sizes of C*n*-125 catalysts on *n*-C7 conversion and yields of various products.

the simultaneous presence of higher C7 conversion and lower selectivities toward cracking and cyclization over this sample under the higher reaction temperatures.

3.3. *Effect of pore curvature on the catalytic performance*

Diffusion problems that are commonly encountered in zeolite micropores can be greatly reduced using catalytic materials with larger pore sizes. All active sites exposed on the pore surface are expected to be readily accessible to the reactant. By varying the pore size, or more precisely, the pore wall surface curvature, we expect to obtain valuable information of how the local curvature affects the catalytic performance in the *n*-C7 hydroconversion. Fig. 9 displays the *n*-C7 conversion and yields of various products versus pore diameters for C*n*-25 samples. For this series samples, a dramatic effect of pore size on the catalytic performance is observed. At lower reaction temperature, below 320 °C, the C7 conversion exhibits a volcano curve. At 300 °C, the lowest value corresponds to C10-25 (18%) and the highest one to C14-25 (58%). When the temperature is above 340 °C, the volcano profile disappears and the maximum conversion is observed on Sample C16-25 (pore diameter is about 2.5 nm). The isomerization yield shows an intriguing phenomenon. A volcano curve with a maximum at around 2.3 nm (yield is three times higher than the lowest) can be observed for the lowest reaction temperature (300 °C); while there is a monotonic rising with pore diameter at 320 °C; it is rather temperature-insensitive at 340 °C, and significantly decreases at higher temperature (360 °C). The evolution of the cracking yield follows the same trend as the *n*-C7 conversion. Although the pore diameter is only 0.8 nm different; the cracking yield at 360 °C of sample C16-25 is about five times larger than that of the Sample C10-25. Volcano curves still exist for the cyclization yield versus pore size. Depending on the reaction temperatures, a maximum exists at either 2.0 or 2.3 nm.

For C*n*-125 samples, despite their similar pore sizes as compared to that of C*n*-25 series, a lower Al content implies a lower active site density on the pore wall surface. The lower catalytic activity obtained on C*n*-125 samples reflects the lower acidity of this series (see Fig. 10). Within the whole temperature range (300–360 °C), only a slight enhancement of *n*-C7 conversion with pore size is observed and the maximum conversion occurs mostly over the samples with the largest pore diameter. For the isomerization yield, an optimal value exists at 2.4 nm between 300 and 320 °C and at 2.7 nm at 340 °C. At 360 °C, a maximum yield at 2.1 nm is observed. In addition, an increasing cracking yield with pore size can be found between 300 and 340 °C. However, a maximum cracking yield is observed for the 2.4 nm sample at 360 °C. For cyclization, smooth volcano profiles are found in the whole temperature range with maximum values at 2.4 nm between 300 and 320 °C and 2.1 nm between 340 and 360 °C. In the view of reaction thermodynamics, the lower temperature favors the formation of isomers while the cracking and cyclization are favored under the elevated temperature, it is readily conceived the lower yield of isomerization at 360 °C over larger pore size samples is associated closely with the formation of much more cracking and cyclization products.

For the isomerization of alkanes over bifunctional catalysts, a well-balanced ratio between acid and metal sites is of great benefit for achieving the desired catalytic performance. Guisnet et al. [41] found, with PtHY catalysts containing less than six acid sites per metallic site, the relative “ideal” reaction situation occurs, that is, *n*-C7 transforms successively into isomers and cracking products. The similar situation was reported by Chaudhari et al. [39] over Al-MCM-41 supported Pt catalysts, the optimum Pt loading for n-hexane isomerization was around 0.3 wt.%, resulting in a ratio of Pt atom to the number of the acid sites of about nine. Under the above optimum conditions, the isomerization occurs through a step-by-step process and the primary reaction products are monobranched isomers. It can be assumed here that the metallic sites are more than sufficient because of the lower aluminum content of Al-MCM-41 materials. Their acidity is rather mild which is similar to that of amorphous aluminosilicates and much lower than that of zeolites such as USY or H-MOR. Thus, it can be expected that the catalytic behavior will mainly depend on the acidic properties of the support.

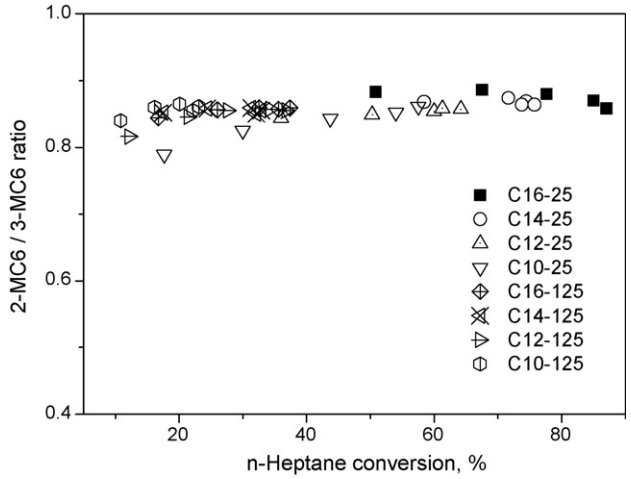

Fig. 11. Influence of *n*-C7 conversion on 2-MC_6/3-MC_6 ratio.

It is well known that the branching of carbeniums or smaller carbeniums and olefins formed by cracking occurs through protonated cyclopropane (PCP) intermediates [42,43]. Therefore, more 3-MC6 (3-methyl-hexane) rather than 2-MC6 (2-methyl-hexane) is expected to be produced in the C7 conversion in the case of no diffusion constraint. It is clear from Fig. 11 that mono-branched 2-MC6/3-MC6 ratio lies between 0.75 and 0.9, indicating that the steric restrictions are negligible for our catalytic systems.

For each series of Al-MCM-41 samples C*n*-25 and C*n*-125, they have different pore sizes but similar number of active centers because of the constant aluminum content. Therefore, their catalytic behaviors are closely related to the pore wall local curvature. For both series, the appearance of maximum *n*-C7 conversion and yield distributions occurring at different pore sizes makes the interpretation of the experimental results rather difficult. The complexity of the catalytic performance with pore size can be partly attributed to the co-existence of different reaction pathways during the formation of isomers, cracking and cyclization products. In addition, thermodynamic limitations have to be considered at higher reaction temperatures.

To reduce the unfavorable effect of hydrocracking when interpreting the curvature effect on selectivities of various products, the *n*-C7 conversion was controlled under a relatively low conversion for all the catalytic runs (~20%) via decreasing the reaction temperature. The relationship between the pore size and selectivity of different products for both series of catalysts is shown in Fig. 12. It is clear that the selectivities vary volcanically as the pore size increases for both series of samples. More significant changes occur over C*n*-25 series, the highest isomerization selectivity is about 20% higher than the lowest one over both series of catalysts while two times and four times for cracking and cyclization selectivities, respectively. For all Al-MCM-41 catalysts, Al sites are uniformly distributed forming isolated Al sites, because the isomorphous substitution was successfully achieved and the high surface area of the support. However, higher Al content results in higher acid density, thereby the local curvature effect being more pronounced as indicated by more remarkable variation of selectivities of isomerization, cracking and cyclization on C*n*-25 samples as a function of the pore diameter. On the contrary, this effect is weakened by the insufficient activation ability of less acid centers for C*n*-125 series.

The *I*/*C* (isomerization/cracking) ratio can be considered as an important index for evaluating the performance of isomerization catalysts. Fig. 13(A) compares the effect of the pore curvature on the *I*/*C* ratio at 20% *n*-C7 conversion. The C*n*-25 samples show an obvious volcano curve with lowest *I*/*C* ratio at 2.0 nm. On the other hand, the *I*/*C* ratio decreases with pore diameter for the C*n*-125 samples with a higher Si/Al ratio, the highest *I*/*C* ratio can be obtained by decreasing the pore size. However, increasing the pore size is required to give better *I*/*C* ratio over C*n*-25 samples under the present conditions.

Due to the weak acidity of the catalysts and the relatively high reaction temperature, cyclization products, mainly aromatics (toluene and benzene), are produced during *n*-C7 hydroconversion. The formation of aromatics as a function of pore diameter is shown in Fig. 13(B). A decreased trend is observed for C*n*-25 samples with maximum selectivity toward aromatics at 1.7 nm. With C*n*-125 series, an obvious volcano curve with the maximum at 2.1 nm is observed as the pore diameter increases. Comparing both series of catalysts, it is clear that higher aromatics selectivity can be achieved with C*n*-125 samples. This behavior is closely related to the low acidity of C*n*-125 samples, which inhibits the formation of the precursors of the carbonaceous compounds. Combined with the trend of cyclization yield versus pore diameter (Figs. 9 and 10), it can be found that aromatics selectivity usually increases with increasing temperature disregarding the pore size and Si/Al ratio.

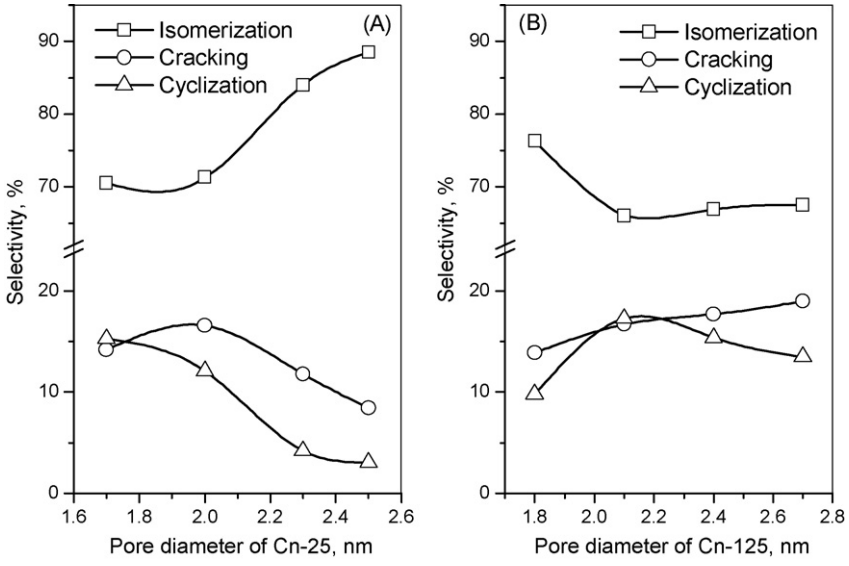

Fig. 12. Influence of pore size on selectivity of various products in *n*-C7 conversion over Pt supported (A) C*n*-25 and (B) C*n*-125 catalysts.

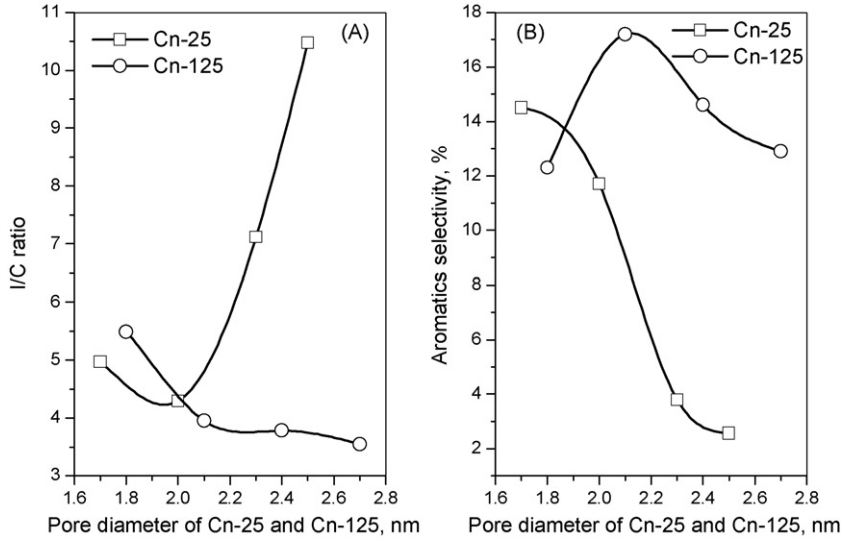

Fig. 13. Influence of pore size on (A) *I*/*C* ratio and (B) aromatics selectivity over C*n*-25 and C*n*-125 catalysts.

The relationship between acidity and catalytic behavior can be easily rationalized for C*n*-25 series. Since C16-25 and C14-25 exhibit higher total acid density and a larger number of stronger acid sites, better C7 conversion is obtained and the isomerization selectivity is also higher than those observed on the two others. Relatively less cracking products forms as the acidity increases, which suggests the metal active sites are well-dispersed over larger pore size samples.

However, the variation of catalytic performances is rather subtle for C*n*-125 series due to their comparable acidity. Although fairly good catalytic conversion can be led to by using the larger pore size materials, the selectivities toward various products are different: excellent isomerization selectivity is found on C10-125, which corresponds the lower cracking and cyclization selectivities (Fig. 12).

Acidity also affects the *I*/*C* ratio. For C*n*-25 series, bigger pore size samples (C14-25 and C16-25) give better *I*/*C* ratio due to much higher acid density and more medium strength acid sites. Moreover, high aromatics selectivity is obtained on samples with lower acidity such as C10-25 and C12-25. For C*n*-125 series, such correlation is lacking due to analogous acidity.

It can be found that pore diameters and the reaction temperature can be utilized to dramatically tune the *n*-C7 conversion, isomerization selectivity, *I*/*C* ratio, and aromatics selectivity. Considering that the formation of reactive intermediates, probably carbenium ions formed over acid sites, plays a crucial role in the isomerization of n-alkanes [44,45]. Therefore, the capability of proton transfer of the catalyst is one of the very important steps determining whether these carbonation active species can be readily produced or not. It can be supposed reasonably that the certain correlation between pore curvature and isomerization reaction is present for the mesoporous Al-MCM-41 used here. Combined other findings of pore wall curvature effect on the catalytic reactivity, selectivity and stability reported for MCM-41 materials, e.g., methanol oxidation over V-MCM-41 [23] and control of cobalt nano-cluster formation in MCM-41 pore [22,46], we can postulate that the local curvature affects the isomerization reaction on the atomic level beyond the steric restriction. The variation of local curvature, although subtle, may generate the catalytically active centers with different strength distributions because of the different T–O–T angles. This effect of surface curvature is strong enough to affect the transfer of those very active species during the reaction, e.g., the proton transfer in this study, the electron transfer in the methanol oxidation and the migration of freshly reduced cobalt atoms in the cobalt nano-cluster formation.

4. Conclusions

Mesoporous molecular sieve Pt/Al-MCM-41 materials with fixed Si/Al ratios but different pore sizes have been synthesized. It is shown by N_2 physisorption, XRD, SEM, TEM, FTIR, NMR, and NH_3-TPD that the Pt/Al-MCM-41 materials are well-ordered aluminosilicates with high level of Al incorporation and mild acidity. Mono-branched 2-MC6/3-MC6 ratio indicates that the steric restrictions are negligible for this catalytic system. By adjusting pore diameter, Al content and reaction temperature, one can achieve high catalytic conversion with desirable production distribution: (1) over C*n*-25 catalysts, a better *n*-C7 conversion and isomerization yield can be obtained with larger pore size samples while a high *I*/*C* ratio and aromatics selectivity over smaller pore size samples. (2) For C*n*-125 catalysts, smaller pore size samples show relatively stable isomerization selectivity but low C7 conversion and isomerization yield as compared to large pore size catalysts. However, these catalysts have better toluene selectivity than C*n*-25 catalysts. These adjustable parameters provide feasible options for designing the novel hydroconversion catalysts.

Acknowledgements

The authors thank AcRF tier 2 (M45120006 ARC 13/07) for providing funding support. The financial support of A*STAR project 062 101 0035 is gratefully acknowledged.

References

[1] I.E. Maxwell, W.H.J. Stork, Stud. Surf. Sci. Catal. 137 (2001) 747.
[2] S.J. Miller, Micropor. Mater. 2 (1994) 439.
[3] P.B. Koriada, J.R. Kiosky, M.Y. Asim, J. Catal. 66 (1980) 290.
[4] M. Tromp, J.A. van Bokhoven, M.T. Garriga Oostenbrink, J.H. Bitter, K.P. de Jong, D.C. Koningsberger, J. Catal. 190 (2000) 209.
[5] A. Chica, A. Corma, J. Catal. 187 (1999) p167.
[6] A. Patrigeon, E. Benazzi, Ch. Travers, J.Y. Bernhard, Catal. Today 65 (2001) 149.
[7] R. Roldán, F.J. Romero, C. Jiménez-Sanchidrián, J.M. Marinas, J.P. Gómez, Appl. Catal. A 288 (2005) 104.
[8] Z.M. Wang, Z.J. Tian, F. Teng, G.D. Wen, Y.P. Xu, Z.S. Xu, L.W. Lin, Catal. Lett. 103 (2005) 109.
[9] M. Höchtl, A. Jentys, H. Vinek, J. Catal. 190 (2000) 419.
[10] J.S. Beck, J.C. Vartuli, W.J. Roth, M.E. Leonowicz, C.T. Kresge, K.D. Schmitt, C.T-W. Chu, D.H. Olson, E.W. Sheppard, S.B. McCullen, J.B. Higgins, J.L. Schlenker, J. Am. Chem. Soc. 114 (1992) 10834.
[11] J.C. Vartuli, T.F. Degnan, Stud. Surf. Sci. Catal. 168 (2007) 837.
[12] A. Corma, D. Kumar, Stud. Surf. Sci. Catal. 117 (1998) 201.
[13] B. Smit, T.L.M. Maesen, Nature 451 (2008) 671.

[14] J. Cejka, B. Wichterlova, Catal. Rev. Sci. Eng. 44 (2002) 375.
[15] Y. Sugi, M. Toba, Catal. Today 19 (1994) 187.
[16] N.Y. Chen, W.E. Garwood, Catal. Rev. Sci. Eng. 28 (1986) 185.
[17] S.M. Csicsery, Zeolite 4 (1984) 202.
[18] E.G. Derouane, J.M. Andre, A.A. Lucas, J. Catal. 110 (1988) 58.
[19] G.L. Haller, J. Catal. 216 (2003) 12.
[20] X. Feng, J.S. Lee, J.W. Lee, J.Y. Lee, D. Wei, G.L. Haller, Chem. Eng. J. 64 (1996) 255.
[21] W.T. Chueh, Ph.D. Dissertation, Yale University, 1998.
[22] D. Ciuparu, Y. Chen, S.Y. Lim, G.L. Haller, L. Pfefferle, J. Phys. Chem. B 108 (2004) 503.
[23] Y.H. Yang, G.A. Du, S.Y. Lim, G.L. Haller, J. Catal. 234 (2005) 318.
[24] Q.H. Tang, C. Wang, S.Q. Hu, H. Sun, Y. Chen, G.L. Haller, Y.H. Yang, Catal. Lett. 117 (2007) 25.
[25] Y. Cesteros, G. Haller, Micropor. Mesopor. Mater. 43 (2000) 171.
[26] E.P. Barrett, L.G. Joyner, P.P. Halenda, J. Am. Chem. Soc. 73 (1951) 373.
[27] M. Kruk, M. Jaroniec, A. Sayari, J. Phys. Chem. B 101 (1997) 583.
[28] K.S.W. Sing, D.H. Everett, R.A.W. Haul, L. Moscou, R. Pierotti, J. Rouquerol, T. Siemienwska, Pure Appl. Chem. 57 (1985) 603.
[29] S. Hitz, R. Prins, J. Catal. 168 (1997) 194.
[30] Z. Luan, H. He, W. Zhou, C.F. Cheng, J. Klinowsiki, J. Chem. Soc., Faraday Trans. 91 (1995) 2955.
[31] J.L. Blin, C. Otjacques, G. Herrier, B.L. Su, Int. J. Inorg. Mater. 3 (2001) 75.
[32] E.M. Flanigen, H. Khatami, H.A. Seymenski, Adv. Chem. Ser. 101 (1971) 201.
[33] C.Y. Chen, H.X. Li, M.E. Davis, Micropor. Mater. 2 (1993) 17.
[34] W. Kolodziejski, A. Corma, M.T. Navarro, J. Perez-Pariente, Solid State Nucl, Magn. Reson. 2 (1993) 253.
[35] Z. Luan, C.F. Cheng, W. Zhou, J. Klinowski, J. Phys. Chem. 99 (1995) 1018.
[36] A. Corma, V. Fornés, M.T. Navarro, J. Pérez-Pariente, J. Catal. 148 (1994) 569.
[37] K.M. Reddy, C. Song, Catal. Lett. 36 (1996) 103.
[38] R. Mokaya, W. Jones, S. Moreno, G. Poncelet, Catal. Lett. 49 (1997) 87.
[39] K. Chaudhari, T.K. Das, A.J. Chandwadkar, S. Svasanker, J. Catal. 186 (1999) 81.
[40] I.E. Maxwell, Catal. Today 1 (1987) 385.
[41] M. Guisnet, F. Alvarez, G. Giannetto, G. Perot, Catal. Today 1 (1987) 415.
[42] G.E. Giannetto, G.R. Perot, M.R. Guisnet, Ind. Eng. Chem. Prod. Res. Dev. 25 (1986) 481.
[43] S.T. Sie, Ind. Eng. Chem. Res. 32 (1993) 403.
[44] J.A. Martens, P.A. Jacobs, Stud. Surf. Sci. Catal. 137 (2001) 633.
[45] R.A. van Santen, Chem. Rev. 95 (1995) 637.
[46] S. Lim, D. Ciupara, Y. Chen, Y.H. Yang, L. Pfefferle, G.L. Haller, J. Phys. Chem. B 109 (2005) 2285.